



**HAL**  
open science

## Mineral dust photochemistry induces nucleation events in the presence of SO<sub>2</sub>

Y. Dupart, S. M. King, B. Nekat, A. Nowak, A. Wiedensohler, H. Herrmann,  
G. David, B. Thomas, Alain Miffre, P. Rairoux, et al.

► **To cite this version:**

Y. Dupart, S. M. King, B. Nekat, A. Nowak, A. Wiedensohler, et al.. Mineral dust photochemistry induces nucleation events in the presence of SO<sub>2</sub>. Proceedings of the National Academy of Sciences of the United States of America, 2012, 109, pp.20842-20847. 10.1073/pnas.1212297109 . hal-00797945

**HAL Id: hal-00797945**

**<https://hal.science/hal-00797945>**

Submitted on 13 Oct 2021

**HAL** is a multi-disciplinary open access archive for the deposit and dissemination of scientific research documents, whether they are published or not. The documents may come from teaching and research institutions in France or abroad, or from public or private research centers.

L'archive ouverte pluridisciplinaire **HAL**, est destinée au dépôt et à la diffusion de documents scientifiques de niveau recherche, publiés ou non, émanant des établissements d'enseignement et de recherche français ou étrangers, des laboratoires publics ou privés.

# Mineral dust photochemistry induces nucleation events in the presence of SO<sub>2</sub>

Yoan Dupart<sup>a</sup>, Stephanie M. King<sup>a,1</sup>, Bettina Nekat<sup>b</sup>, Andreas Nowak<sup>b,2</sup>, Alfred Wiedensohler<sup>b</sup>, Hartmut Herrmann<sup>b</sup>, Gregory David<sup>c</sup>, Benjamin Thomas<sup>c</sup>, Alain Miffre<sup>c</sup>, Patrick Rairoux<sup>c</sup>, Barbara D'Anna<sup>a</sup>, and Christian George<sup>a,3</sup>

<sup>a</sup>Université de Lyon 1, Lyon, Institut de Recherches sur la Catalyse et l'Environnement de Lyon, Centre National de la Recherche Scientifique (CNRS), Unité Mixte de Recherche (UMR) 5256, Villeurbanne, F-69626, France; <sup>b</sup>Leibniz Institut for Tropospheric Research, Permoserstr. 15, 04318 Leipzig, Germany; and <sup>c</sup>Institut Lumière Matière, UMR5306 Université Lyon 1-CNRS, Université de Lyon, 69622 Villeurbanne cedex, France

Edited by Mark H. Thiemens, University of California at San Diego, La Jolla, CA, and approved November 2, 2012 (received for review July 18, 2012)

**Large quantities of mineral dust particles are frequently ejected into the atmosphere through the action of wind. The surface of dust particles acts as a sink for many gases, such as sulfur dioxide. It is well known that under most conditions, sulfur dioxide reacts on dust particle surfaces, leading to the production of sulfate ions. In this report, for specific atmospheric conditions, we provide evidence for an alternate pathway in which a series of reactions under solar UV light produces first gaseous sulfuric acid as an intermediate product before surface-bound sulfate. Metal oxides present in mineral dust act as atmospheric photocatalysts promoting the formation of gaseous OH radicals, which initiate the conversion of SO<sub>2</sub> to H<sub>2</sub>SO<sub>4</sub> in the vicinity of dust particles. Under low dust conditions, this process may lead to nucleation events in the atmosphere. The laboratory findings are supported by recent field observations near Beijing, China, and Lyon, France.**

OH production | photocatalysis | SO<sub>2</sub> nucleation | LIDAR | atmospheric optics

**M**ineral dust contributes to a major fraction of the global coarse mode aerosol load, with an emission rate into the atmosphere currently estimated at 1,000–3,000 Tg per year (1) from the Earth's surface. Mineral dust particles have a significant impact on the Earth's radiation budget by scattering light and affecting cloud formation (2). Smaller dust particles with longer residence times may be transported over large distances, affecting the chemical composition of the atmosphere, as well as continental and oceanic nutrient levels. During advection, mineral dust particles interact with sulfur dioxide (SO<sub>2</sub>) and other atmospheric trace gases. Current knowledge shows that sulfur dioxide adsorbs onto many of the components of mineral dust as adsorbed sulfite, which can be oxidized to sulfate (3), for example, by ozone (4), by surface defect sites, or by photooxidation (5–8). These previous studies (and references therein) clearly demonstrated that particulate sulfate is the end product of the SO<sub>2</sub> chemistry on dust surfaces (9). Korhonen et al. (10) also showed that, despite the existence of an energy barrier, ternary heterogeneous nucleation of water, sulfuric acid, and ammonia is a possible pathway leading to sulfate coating of mineral aerosol particles. However, the specificity and impact of the photochemical reaction sequence involving SO<sub>2</sub> and low dust loadings has not yet been described.

Recent studies by Ndour and coworkers (11–13) highlighted the importance of dust photochemistry under atmospheric conditions. Under UV light, TiO<sub>2</sub> and Fe<sub>2</sub>O<sub>3</sub>, which are common components of mineral dust, photoenhance the uptake of trace gases on dust surfaces via their photocatalytic activity, generating electron-hole pairs that lead to the formation of OH<sup>•</sup>, HO<sub>2</sub><sup>•</sup>, and other radicals that are subsequently available for oxidation and reduction reactions (14, 15). It is generally assumed that photocatalysis is a surface-mediated process, where only surface reactions are taking place (16). However, the possibility exists for these radicals to desorb and initiate gas-phase chemistry in the vicinity of the surface (17–19), thereby changing the chemistry and impact of atmospheric dust. In this work, we present the observation of new particle formation (NPF) by considering an

alternative pathway for H<sub>2</sub>SO<sub>4</sub> particle nucleation in the troposphere. More specifically, a reaction scheme is deduced along with its quantitative equation rate (Eq. 1), relating SO<sub>2</sub> and gas phase OH, through a photocatalytic surface mechanism based on the semiconductor properties of dust particles.

## Results and Discussion

We report laboratory experiments showing that the interaction of SO<sub>2</sub> with dust particles in an aerosol flow tube (AFT) (*Materials and Methods* and Fig. S1) under UV light resulted systematically in NPF [i.e., a large concentration of nanometer-sized particles (diameter of 10 nm or less) was measured at the exit of the AFT (Fig. 1)]. In contrast, the total particle number concentration and number size distribution were constant under dark conditions. The nucleation events were clearly observed for Fe<sub>2</sub>O<sub>3</sub> and for Arizona test dust (ATD) (containing traces of Fe<sub>2</sub>O<sub>3</sub> and TiO<sub>2</sub>; Table S1–S3) and only in the presence of water vapor, gaseous SO<sub>2</sub>, and UV irradiation (Fig. 2). The absence of any one of these inhibited the nucleation.

The particle number concentration exiting the AFT after nucleation increased with increasing photon flux (Fig. 1). A similar trend was observed with increasing relative humidity (RH) and increasing SO<sub>2</sub> concentration. On the other hand, the particle number concentration decreased with increasing residence time (Fig. 2), which is consistent with a growing condensational sink.

The possibility that particulate sulfate is produced following photoinduced reaction of SO<sub>2</sub> on the dust proxies was investigated by using the AMS and ion chromatographic analyses (881 Compact IC; Metrohm). None of these two approaches could confirm the production of significant amount of particulate sulfate under the specific experimental conditions (i.e., low dust surface to prevent adsorption of the NPF precursors).

Control experiments were conducted by substituting the mineral dust proxies with NaCl or with SiO<sub>2</sub>, two photochemically unreactive proxies at the relevant wavelengths. In both cases, nucleation was not observed.

These observations indicate that: (i) particle nucleation is not attributable to any artifact or impurities initiating gas phase

Author contributions: H.H., A.M., P.R., B.D., and C.G. designed research; Y.D., S.M.K., B.N., A.N., A.W., H.H., G.D., B.T., A.M., P.R., B.D., and C.G. performed research; C.G. contributed new reagents/analytic tools; Y.D., S.M.K., B.N., A.N., A.W., H.H., G.D., B.T., A.M., P.R., B.D., and C.G. analyzed data; and Y.D., S.M.K., B.N., H.H., G.D., B.T., A.M., P.R., B.D., and C.G. wrote the paper.

The authors declare no conflict of interest.

This article is a PNAS Direct Submission.

<sup>1</sup>Present address: Department of Chemistry, University of Copenhagen, DK-2100 Copenhagen, Denmark.

<sup>2</sup>Present address: Physikalisch-Technische Bundesanstalt (PTB), Analytics and Thermodynamic State Behaviour of Gases Department, 38116 Braunschweig, Germany.

<sup>3</sup>To whom correspondence should be addressed. E-mail: Christian.George@irclyon.univ-lyon1.fr.

This article contains supporting information online at [www.pnas.org/lookup/suppl/doi:10.1073/pnas.1212297109/-DCSupplemental](http://www.pnas.org/lookup/suppl/doi:10.1073/pnas.1212297109/-DCSupplemental).





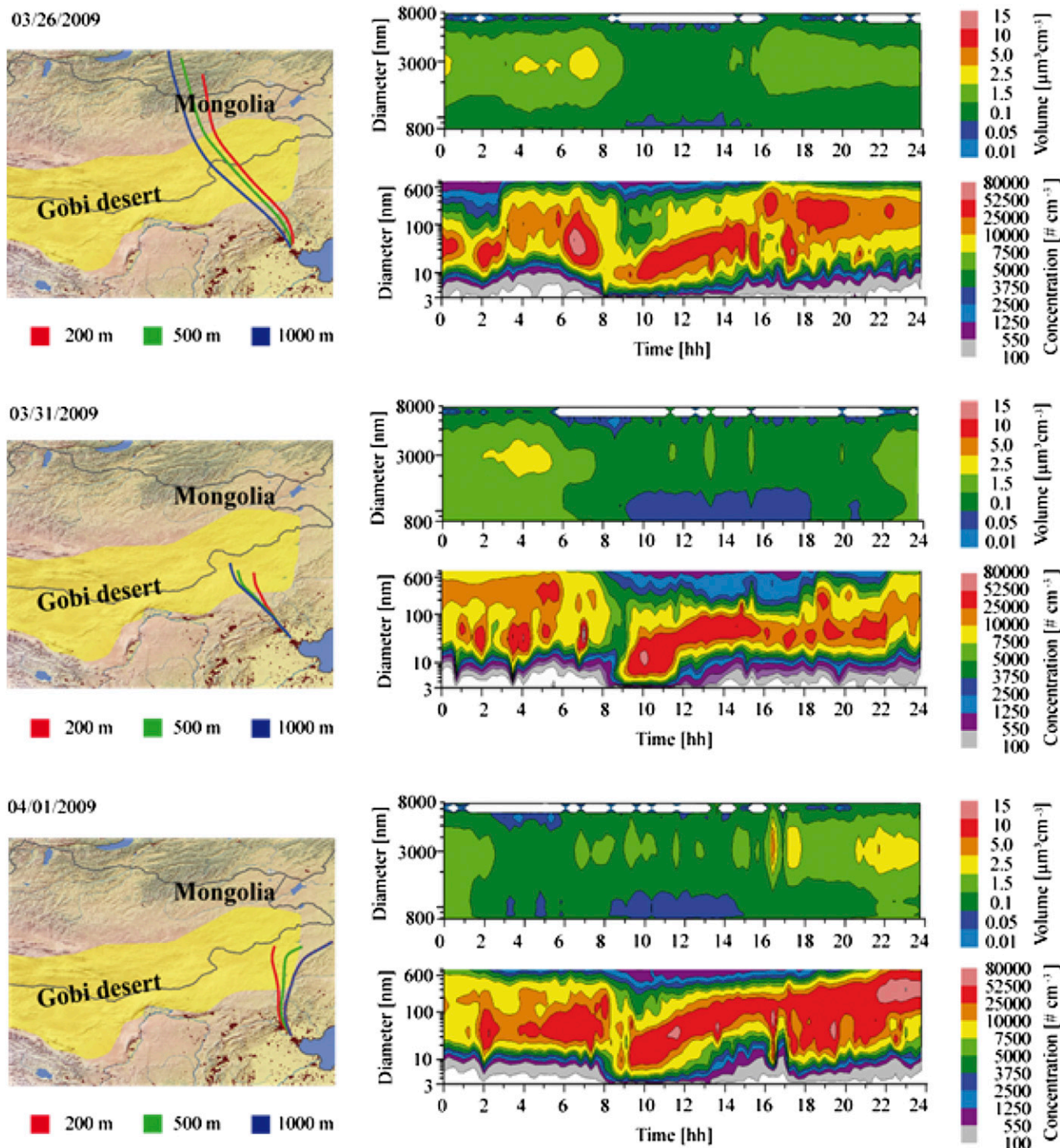


**Fig. 4.** Ground-based in situ measurements conducted at the Wuqing meteorological station, China ( $39^{\circ}23'9''\text{N}$ ,  $117^{\circ}1'26''\text{E}$ ), on a) the seven NPF days. Twenty-four-hour back-trajectories were calculated with the National Oceanic and Atmospheric Administration (NOAA) HYSPLIT (Hybrid Single-Particle Lagrangian Integrated Trajectories, version 4.8) model at starting heights of 200, 500, and 1,000 m and a starting time of 08:00 hours local time [coordinated universal time (UTC) plus 8 h] (left column). The right column shows particle-volume distribution in the size range between 0.8–8  $\mu\text{m}$ , indicating the presence of coarse particles (upper graphs); and particle-number concentrations for particle diameters between 3 and 800 nm (data ranges are color-coded) as a function of local time of day (x axis) and the particle diameter (y axis) (lower graphs).

other gases than just sulfuric acid. Kirkby et al. (26) very recently showed that, in the boundary layer, ammonia mixing ratios of 100 parts per trillion by volume (pptv), or less, increase the nucleation rate of sulfuric acid particles more than 100–1,000-fold. In a similar vein, Bzdek et al. (27), using a nano-AMS (NAMS), have

shown that sulfuric acid accounts for 29–46% of the total mass growth of 20- to 25-nm particles, with strong contributions from ammonium, nitrate, and organics.

Because accurate UV-polarization light detection and ranging (LIDAR) remote sensing is sensitive to both ultrafine and fine

particles in the free troposphere (ref. 28 and *SIText*), we performed a UV-polarization LIDAR experiment to evaluate the particulate matter UV-backscattering coefficient  $\beta$ , which is proportional to the particle number concentration for both spherical [e.g., nucleated particles ( $\beta_s$ )] and nonspherical (dust) ( $\beta_d$ ) particles by using the methodology developed by Miffre et al. (28) during a long-range Saharan dust episode in the free troposphere above Lyon, France. Fig. 5A displays  $\beta_s$  as a function of the solar UV irradiance during sunrise, while the dust particle concentration and RH remained constant. Within our error bars,  $\beta_s$  increases with solar UV irradiance, whereas the nonspherical particle concentration is low. During the dust episode, nonspherical particles corresponded to dust particles. Fig. 5B is a scatter plot showing  $\beta_s$  as a function of  $\beta_d$  during daylight and nighttime hours. During daylight hours, a maximum in  $\beta_s$  is observed at the lowest  $\beta_d$  values, in contrast to nighttime observations. We deduce that fine and ultrafine particles are more abundant when the numbers of nonspherical dust particles decreases, which indirectly supports the reported laboratory observations.

The combined laboratory and field observations presented here clearly provide evidence that the semiconductor properties of atmospheric dust particles lead to new chemical properties affecting aerosol formation, associated with dust, in the troposphere.

## Materials and Methods

**AFT.** The experiments were performed at IRCELYON under atmospheric conditions (298 K; 1 atm) in a temperature-controlled horizontal aerosol flow tube (AFT) made of Pyrex with a length of 180 cm and an inner diameter of 6 cm (29) (Fig. S1). The AFT was housed in an opaque chamber of equal length, which was equipped with five coaxially mounted lamps (CLEO 80W; Philips) that provided continuous UV irradiation (300- to 420-nm wavelength) from  $0.75 \times 10^{15}$  to  $3.77 \times 10^{15}$  photons per square centimeter per second. The concentration of  $\text{SO}_2$  (ranging from 35 to 500 ppbv) and the RH were controlled at the exit of the AFT. The dust particle residence time was between 15 and 510 s.

Upon exiting the AFT, the aerosol stream is sent to a scanning mobility particle sizer (SMPS) (TSI). In some tests, an Aerodyne compact time-of-flight (C-TOF) (ToFWerk) aerosol mass spectrometer (AMS) (Aerodyne) was used to identify particle bound sulfate.

Two proxies for mineral dust were probed in this study, iron oxide ( $\text{Fe}_2\text{O}_3$ , <5  $\mu\text{m}$ ; Sigma-Aldrich) and ATD (A1 Ultrafine test dust; Powder Technology) (30). Iron oxide particles were aerosolized from a 150-g powder deposit in a bottle vibrating at a frequency of 80 Hz by means of a loudspeaker. ATD

particles were generated by mechanically mixing 50 g of ATD powder with a magnetic stirrer into a small bottle of glass that was continuously purged with an air or nitrogen flow. In both cases, large particles (>250 nm) were removed by deposition in a dead volume placed in front of the reaction flow tube. The particles in the AFT are, therefore, smaller than those typically found in the atmosphere, but this step was necessary to minimize wall effects attributable to particle deposition.

In the AFT, the particle-number concentration was kept stable over time within fluctuations below 10% for iron oxide particle concentrations of  $400 \pm 30 \text{ cm}^{-3}$ . The same stability was observed for ATD particles with concentrations ranging from 140 to  $20,000 \text{ cm}^{-3}$ . The injected iron oxide and ATD particles were polydispersed, with iron oxide particle diameters ranging from 50 to 180 nm and reaching a maximum at 100 nm, and with ATD particle diameters ranging from 30 to 120 nm and reaching a maximum at 60 nm.

**Field Measurements.** Observations from two separate field measurements performed during dust episodes support the laboratory findings of this study. The first ground-based campaign took place from March 2 to April 4, 2009, near Beijing, China, and the second remote-sensing campaign took place on July 9, 2010, in Lyon, France.

**Ground-Based Measurements in China.** Ground-based in situ measurements were conducted at the Wuqing meteorological station ( $39^\circ 23' 9'' \text{N}$ ,  $117^\circ 1' 26'' \text{E}$ ), located between Beijing to the Northwest and Tianjin to the South. The measurement period is characterized by frequent dust events transporting large amounts of mineral dust from the Gobi desert (31, 32) to Beijing and to the North China Plain. The number concentration of particles was recorded by a tandem differential mobility particle sizer (TDMPs) with mobility diameters from 3 to 800 nm, whereas an aerodynamic particle sizer (APS) (model 3310; TSI) was used for larger particles (with aerodynamic diameters up to 20  $\mu\text{m}$ ). A high-volume filter sampler (DIGITEL DHA-80; Riemer Electronics) equipped with a  $\text{PM}_{10}$  inlet was used for particle sampling. The filter samples were analyzed as described by van Pinxteren et al. (33).

**LIDAR Remote-Sensing Measurement in France.** The ability to detect very low particle UV-backscattering coefficient with Lyon UV-LIDAR has been demonstrated in terms of optics (34), field applications (35), and environmental geophysical purposes (28), in agreement with optical scattering theory (28, 36). This state of the art has been achieved in the UV-spectral range through sensitive and accurate range-resolved polarization backscattering measurements [particle depolarization ratio as low as  $6 \times 10^{-3}$ , known with a 2% accuracy, because of very low  $4 \times 10^{-8}$  polarization cross-talks (34)]. Hence, a nonambiguous remote-sensing observation of both spherical (s) and

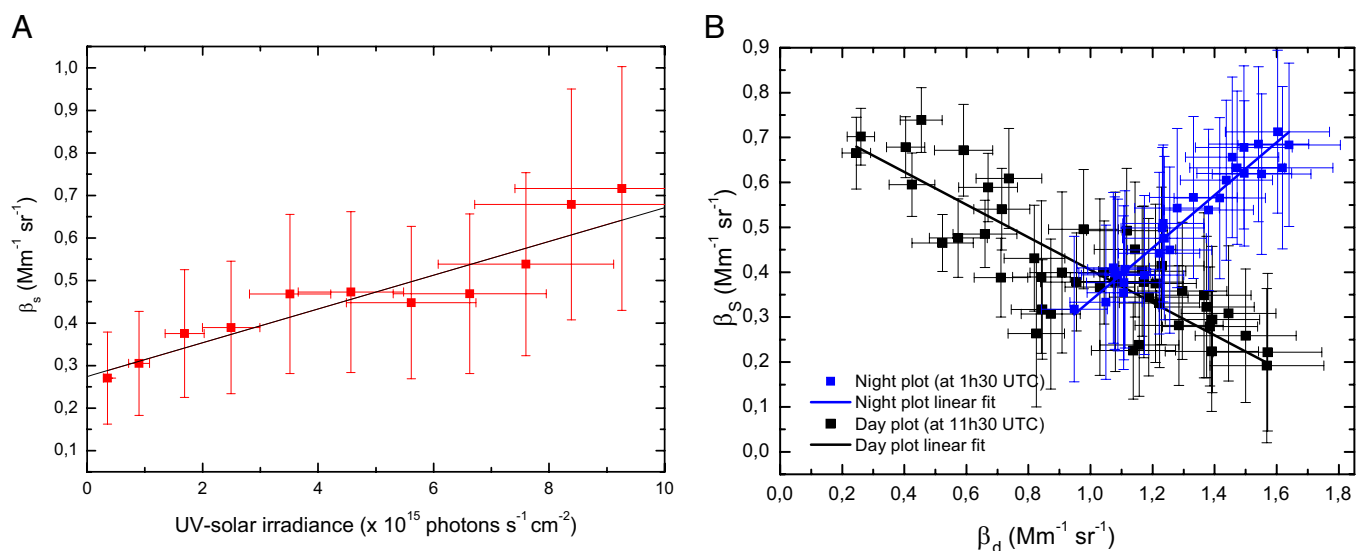


**Fig. 5.** LIDAR remote-sensing experiments performed at Lyon, France, on July 9, 2010, during a long-range Saharan dust episode. (A) Retrieved spherical particle backscattering coefficient  $\beta_s$  as a function of the solar UV irradiance during sunrise while the dust particle concentration and RH remained constant. (B) Scatter plot of the backscattering coefficient  $\beta_s$  as a function of  $\beta_d$  showing negative correlation during daylight hours (black) and positive correlation during nighttime hours (blue).

nonspherical (ns) atmospheric particles scattering has been achieved (34) and a very low detection threshold ( $\beta_{p,lim} = 1.0 \times 10^{-7} \text{ m}^{-1} \text{ sr}^{-1}$ ) has been obtained for s-particle backscattering in the UV range ( $\lambda = 355 \text{ nm}$ ). Such a low value for the s-particle backscattering coefficient makes the detection of fine and ultrafine particle possible (ref. 34 and *SI Materials and Methods*). During the July 9, 2010 dust episode, above Lyon, ns particles were attributed to highly irregularly shaped dust (d) particles, as confirmed by Fig. 53.

Fig. 5A plots the LIDAR s-particle backscattering coefficient at 3.2-km altitude, on July 9, 2010 during sunrise as a function of the solar UV irradiance. The UV irradiance (in photons per second per square centimeter) illuminating the dust particles at a 3.2-km altitude has been evaluated by considering the Sun as a blackbody, applying the single-scattering atmosphere radiative-transfer formalism to consider the solar light extinction from the top of the atmosphere to the dust particles altitude. This extinction depends on the solar zenith angle and, consequently, on the local solar

angle. Fig. 5A shows that whereas the dust particle concentration and RH remained constant, for UV irradiances similar to those observed in the laboratory, the  $\beta_s$ -backscattering coefficient increases with increasing solar UV irradiance. As shown in *SI Text*, the corresponding mean NPF concentration is in the same range as those observed during the NPF process in the laboratory experiment.

**ACKNOWLEDGMENTS.** We thank Dr. Maria-Eugenia Monge for helpful discussions and support and Pascale Mascunan for the ICP analysis. Support by the French-German atmospheric research program [CNRS–Institut national des sciences de l’Univers/Deutsches Forschungsgemeinschaft (DFG)], Agence Nationale de la Recherche Grant PHOTODUST, the regional Rhône-Alpes environment research program, Seventh Framework Programme (FP7) Project DFG-LEFE, PEGASOS [European Union–FP7 Project Grant 265307], and the DFG HaChi project.

- Tegen I, Schepanski K (2009) The global distribution of mineral dust. *IOP Conf Ser Earth Environ Sci* 7:012001.
- Haywood J, Boucher O (2000) Estimates of the direct and indirect radiative forcing due to tropospheric aerosols: A review. *Rev Geophys* 38(4):513–543.
- Higashi M, Takahashi Y (2009) Detection of S(IV) species in aerosol particles using XANES spectroscopy. *Environ Sci Technol* 43(19):7357–7363.
- Usher CR, Al-Hosney H, Carlos-Cuellar S, Grassian VH (2002) A laboratory study of the heterogeneous uptake and oxidation of sulfur dioxide on mineral dust particles. *J Geophys Res* 107:4713.
- Baltrusaitis J, Cwiertny DM, Grassian VH (2007) Adsorption of sulfur dioxide on hematite and goethite particle surfaces. *Phys Chem Chem Phys* 9(41):5542–5554.
- Cwiertny DM, Young MA, Grassian VH (2008) Chemistry and photochemistry of mineral dust aerosol. *Annu Rev Phys Chem* 59:27–51.
- Nanayakkara CE, Pettibone J, Grassian VH (2012) Sulfur dioxide adsorption and photooxidation on isotopically-labeled titanium dioxide nanoparticle surfaces: Roles of surface hydroxyl groups and adsorbed water in the formation and stability of adsorbed sulfite and sulfate. *Phys Chem Chem Phys* 14(19):6957–6966.
- Baltrusaitis J, Jayaweera PM, Grassian VH (2010) Sulfur dioxide adsorption on TiO<sub>2</sub> nanoparticles: Influence of particle size, coadsorbates, sample pretreatment, and light on surface speciation and surface coverage. *J Phys Chem C* 115(2):492–500.
- Ullerstam M, Vogt R, Langer S, Ljungstrom E (2002) The kinetics and mechanism of SO<sub>2</sub> oxidation by O<sub>3</sub> on mineral dust. *Phys Chem Chem Phys* 4(19):4694–4699.
- Korhonen H, et al. (2003) Heterogeneous nucleation as a potential sulphate-coating mechanism of atmospheric mineral dust particles and implications of coated dust on new particle formation. *J Geophys Res* 108(D17):4546.
- Ndour M, et al. (2009) Photochemistry of mineral dust surface as a potential atmospheric renoxification process. *Geophys Res Lett* 36:L05816.
- Ndour M, et al. (2008) Photoenhanced uptake of NO<sub>2</sub> on mineral dust: Laboratory experiments and model simulations. *Geophys Res Lett* 35(5):L05812.
- Ndour M, Nicolas M, D’Anna B, Ka O, George C (2009) Photoreactivity of NO<sub>2</sub> on mineral dusts originating from different locations of the Sahara desert. *Phys Chem Chem Phys* 11(9):1312–1319.
- Lee MC, Choi W (2002) Solid phase photocatalytic reaction on the soot/TiO<sub>2</sub> interface: The role of migrating OH radicals. *J Phys Chem B* 106(45):11818–11822.
- Park JS, Choi W (2004) Enhanced remote photocatalytic oxidation on surface-fluorinated TiO<sub>2</sub>. *Langmuir* 20(26):11523–11527.
- Shiraishi Y, Hirai T (2008) Selective organic transformations on titanium oxide-based photocatalysts. *J Photochem Photobiol C* 9(4):157–170.
- Park JS, Choi WY (2005) Remote photocatalytic oxidation mediated by active oxygen species penetrating and diffusing through polymer membrane over surface fluorinated TiO<sub>2</sub>. *Chem Lett* 34(12):1630–1631.
- Tatsuma T, Tachibana S-i, Fujishima A (2001) Remote oxidation of organic compounds by UV-irradiated TiO<sub>2</sub> via the gas phase. *J Phys Chem B* 105(29):6987–6992.
- Kubo W, Tatsuma T (2006) Mechanisms of photocatalytic remote oxidation. *J Am Chem Soc* 128(50):16034–16035.
- Zhang R, Khalizov A, Wang L, Hu M, Xu W (2012) Nucleation and growth of nanoparticles in the atmosphere. *Chem Rev* 112(3):1957–2011.
- Berndt T, et al. (2008) SO<sub>2</sub> oxidation products other than H<sub>2</sub>SO<sub>4</sub> as a trigger of new particle formation. Part 1: Laboratory investigations. *Atmos Chem Phys Discuss* 8:9761–9782.
- Laaksonen A, et al. (2008) SO<sub>2</sub> oxidation products other than H<sub>2</sub>SO<sub>4</sub> as a trigger of new particle formation. Part 2: Comparison of ambient and laboratory measurements, and atmospheric implications. *Atmos Chem Phys Disc* 8:9673–9695.
- Sipilä M, et al. (2010) The role of sulfuric acid in atmospheric nucleation. *Science* 327(5970):1243–1246.
- Wang W, et al. (2008) Aircraft measurements of vertical ultrafine particles profiles over Northern China coastal areas during dust storms in 2006. *Atmos Environ* 42(22):5715–5720.
- Kulmala M, Pirjola L, Makela JM (2000) Stable sulphate clusters as a source of new atmospheric particles. *Nature* 404(6773):66–69.
- Kirkby J, et al. (2011) Role of sulphuric acid, ammonia and galactic cosmic rays in atmospheric aerosol nucleation. *Nature* 476(7361):429–433.
- Bzdek BR, Zordan CA, Pennington MR, Luther GW, 3rd, Johnston MV (2012) Quantitative assessment of the sulfuric acid contribution to new particle growth. *Environ Sci Technol* 46(8):4365–4373.
- Miffre A, David G, Thomas B, Rairoux P (2011) Atmospheric non-spherical particles optical properties from UV-polarization lidar and scattering matrix. *Geophys Res Lett* 38, L16804.
- Monge ME, et al. (2012) Alternative pathway for atmospheric particles growth. *Proc Natl Acad Sci USA* 109(18):6840–6844.
- Wagner C, Schuster G, Crowley JN (2009) An aerosol flow tube study of the interaction of N<sub>2</sub>O<sub>5</sub> with calcite, Arizona dust and quartz. *Atmos Environ* 43(32):5001–5008.
- Wang Q, et al. (2011) Mixing of dust with pollution on the transport path of Asian dust—revealed from the aerosol over Yulin, the north edge of Loess Plateau. *Sci Total Environ* 409(3):573–581.
- Zhang R, Han Z, Cheng T, Tao J (2009) Chemical properties and origin of dust aerosols in Beijing during springtime. *Particuology* 7(1):61–67.
- van Pinxteren D, et al. (2009) Size- and time-resolved chemical particle characterization during CAREBeijing-2006: Different pollution regimes and diurnal profiles. *J Geophys Res* 114:D00G09.
- David G, Miffre A, Thomas B, Rairoux P (2012) Sensitive and accurate dual-wavelength polarization Lidar for remote sensing of tropospheric aerosols. *Appl Phys B* 108:197–216.
- Miffre A, et al. (2012) Interpretation of accurate UV polarization lidar measurements: Application to volcanic ash number concentration retrieval. *J Atmos Ocean Technol* 29(4):558–568.
- Veselovskii I, et al. (2010) Application of randomly oriented spheroids for retrieval of dust particle parameters from multiwavelength lidar measurements. *J Geophys Res* 115:D21203.

# Supporting Information

Dupart et al. 10.1073/pnas.1212297109

## Materials and Methods

**AFT.** The experiments were performed at IRCELYON under atmospheric conditions (298 K; 1 atm) in a temperature-controlled horizontal AFT made of Pyrex having a length of 180 cm and an inner diameter of 6 cm (1) (Fig. S1). The AFT was housed in an opaque chamber of equal length, which was equipped with five coaxially mounted lamps (CLEO 80W; Philips) that provided continuous UV irradiation (300- to 420-nm wavelength) from  $0.75 \times 10^{15}$  to  $3.77 \times 10^{15}$  photons per square centimeter per second. The concentration of SO<sub>2</sub> (ranging from 35 to 500 ppbv) and the RH were controlled at the exit of the flow tube. Dust particles were introduced in a carrier gas through a horizontal injector, the position of which was shifted to produce variations in the dust particle residence time between 15 and 510 s.

Upon exiting the AFT, the aerosol stream is sent to a Scanning Mobility Particle Sizer (SMPS) consisting of a differential mobility analyzer (model 3081; TSI) and a condensation particle counter (models 3776; TSI) to measure particle size distribution and concentration. In some tests, an Aerodyne compact time-of-flight (C-TOF) (Tofwerk) AMS (Aerodyne) was used to identify particulate bound sulfate. This instrument measures only the non-refractive portion of the aerosols but is sensitive to sulfate. The AMS analysis provides a mass spectrometric fingerprint of the chemical composition. The aerosol is flash vaporized at 873 K and ionized by electron impact at 30 or 70 eV. The low-energy ionization is used to decrease fragmentation and improve the observation of peaks with higher  $m/z$ . Finally, an ion guide transfers the positively charged ions into the compact orthogonal extraction time-of-flight MS.

Two proxies for mineral dust were probed in this study, iron oxide (Fe<sub>2</sub>O<sub>3</sub>, <5 μm; Sigma-Aldrich) and ATD (A1 Ultrafine test dust; Powder Technology) (2). Iron oxide particles were aerosolized from a 150-g powder deposit in a bottle that was vibrated at a frequency of 80 Hz by means of a loudspeaker. ATD particles were generated by mechanically mixing 50 g of ATD powder with a magnetic stirrer into a small bottle of glass that was continuously purged with an air or nitrogen flow. In both cases, larger particles (>250 nm) were removed by deposition in a dead volume placed in front of the reaction flow tube. The particles in the AFT are, therefore, smaller than those typically found in the atmosphere, but this step was necessary to avoid potential wall effects due to particle deposition.

In the AFT, the particle-number concentration was kept stable over time within fluctuations below 10% for iron oxide particle concentrations of  $400 \pm 30 \text{ cm}^{-3}$ . The same stability was observed for ATD particles with concentrations ranging from 140 to 20,000 cm<sup>-3</sup>. The injected iron oxide and ATD particles were polydispersed, with iron oxide particle diameters ranging from 50 to 180 nm and reaching a maximum at 100 nm and with ATD particle diameters ranging from 30 to 120 nm and reaching a maximum at 60 nm.

**Chemicals.** ATD (Powder Technology) and iron oxide (Fe<sub>2</sub>O<sub>3</sub>) (Sigma-Aldrich) were used as purchased. These commercial samples were nevertheless chemically characterized as shown below.

**Field Measurements.** Observations from two separate field measurements performed during dust episodes support the laboratory findings of this study. The first ground-based campaign took place from March 2 to April 4, 2009, near Beijing, China, and the second remote sensing campaign took place on July 9, 2010 in Lyon, France.

**Ground-Based Measurements in China.** Ground-based in situ measurements were conducted at the Wuqing meteorological station (39°23'9"N, 117°1'26"E), located between Beijing to the Northwest and Tianjin to the South. The measurement period was characterized by frequent dust events transporting large amounts of mineral dust from the Gobi desert (3, 4) to Beijing and to the North China Plain. The number concentration of particles was recorded by a tandem differential mobility particle sizer (TDMPS) with mobility diameters from 3 to 800 nm, whereas an APS (model 3310; TSI) was used for larger particles (with aerodynamic diameters up to 20 μm). A high-volume filter sampler (DIGITEL DHA-80; Riemer Electronics) equipped with a PM<sub>1</sub> inlet was used for particle sampling. The filter samples were analyzed as described in van Pinxteren et al. (5).

To distinguish between dust and nondust events, the 24-h average mass concentrations (TSPs, PM<sub>1</sub>, and PM<sub>10</sub>) were calculated from the combined TDMPS and APS data, assuming an average particle density of 1.45 g·cm<sup>-3</sup>. Higher TSP mass concentrations (TSP ≤ 20 μm) are indications for dust events because larger particles contribute more to the mass concentration than smaller particles. TSP mass concentrations were highest on all pre-NPF days during the campaign, with only one exception, which was attributable to technical problems with the TDMPS. In contrast, the lowest TSP mass concentrations were detected on NPF days. These observations indicate the presence of mineral dust at the location 1 d before a nucleation event occurs. This is further supported by the observed ratio of PM<sub>1</sub> to PM<sub>10</sub>. Assuming that submicron particles are mainly of secondary origin and that most of the larger particles originate from primary sources, such as the resuspension of crust material (e.g., mineral dust), it may be inferred that a smaller PM<sub>1</sub>-to-PM<sub>10</sub> ratio implies a higher dust fraction. Therefore, the significantly lower PM<sub>1</sub>-to-PM<sub>10</sub> ratio observed on all pre-NPF days (Table S4) suggests higher dust content in the atmosphere immediately preceding a nucleation event. These analyses agree with those from laboratory observations, which imply that NPF is most significant at the end of a dust event.

Twenty-four-hour back-trajectories were also calculated with the NOAA HYSPLIT model (Hybrid Single-Particle Lagrangian Integrated Trajectories version 4.8) at starting heights of 200, 500, and 1,000 m and a starting time of 0800 hours local time (UTC plus 8 h). These were used to assess the origin of particles at the measurement location when particle nucleation is first observed (between 0700 and 1000 hours local time; Fig. 4 and Fig. S2, left column). On all NPF days, air parcels originated from the northwest and passed the Gobi desert regions of Mongolia and North China (Fig. 4 and Fig. S2, left column). The back-trajectories in Fig. 4 and Fig. S2, left column, show the influence of dust source contributions from the Gobi desert (yellow area). In the right column, the time-dependent number concentration plots are shown for days when nucleation was observed (right column, lower plots). Above these plots, the time-resolved volume distributions for particles having diameters between 0.8 and 8 μm are shown. These above plots clearly indicate that surprisingly large amounts of dust particles are present at the time that nucleation is first observed (i.e., in the morning hours). Coarse-mode particle volumes are in the range of  $1.5\text{--}1.7 \times 10^{-6} \text{ cm}^{-3} \cdot \text{m}^{-3}$  averaged over the 3 h (0600 to 0900 hours local time) before NPF occurs.

**LIDAR Remote-Sensing Measurement in France.** It is generally considered that ultrafine particles cannot be observed with optical scattering based on LIDAR. Nevertheless, ultrafine particles,

despite their very low sizes, may strongly contribute to optical scattering when they are numerous, as implied by atmospheric molecular scattering, and are responsible for the blue color of the sky. NPF events, which are clearly visible in the Beijing so-called banana plots, have been used as a particle size distribution (PSD) for simulating a LIDAR nucleation event, because as detailed below, the retrieved dust and spherical-particle concentration are in the same range. In our polarization LIDAR experiment, the  $\beta_s$  coefficient corresponding to the ground-based Beijing measurements has been derived by using the Lorentz–Mie theory, suitable for spherical particles. For the middle banana-plot in Fig. 4, after 1000 hours local time, the observed increase in  $\beta_p$  during the NPF event is above the  $\beta_{p,\text{lim}}$ -detection threshold of  $s$  particles and is, therefore, detectable with backscattering UV-polarization LIDAR. Particles having a diameter between 3 and 800 nm exhibit an increase in the  $\beta_s$  backscattering, which grows up to  $3.0 \times 10^{-7} \text{ m}^{-1} \text{ sr}^{-1}$  during the NPF event, which is above our UV-polarization detection threshold of  $1.0 \times 10^{-7} \text{ m}^{-1} \text{ sr}^{-1}$ . Moreover, a  $\beta_s$  increase up to  $7.0 \times 10^{-7} \text{ m}^{-1} \text{ sr}^{-1}$  is obtained for particle diameters between 3 and 200 nm, corresponding to the NPF process (6).

During the July 9, 2010 episode, nonspherical particles were attributed to dust particles, as confirmed by the 7-d FLEXTRA back-trajectories originating from the Saharan dust region, for altitudes between 3 and 6 km above mean sea level (Fig. S1). Then, in Fig. S2, we represent the LIDAR vertical  $s$ - and  $d$ -particle backscattering-coefficient profiles that are plotted for July 9, 2010, at Lyon during nighttime and daytime, for altitudes

between 3.2 and 5 km above mean sea level. These vertical profiles have been derived by applying the methodology published by Miffre et al. (7). Finally, these vertical profiles are used to compute the scatter plot in Fig. 5.

Finally, to compare with the laboratory observation, we evaluated the mean NPF concentration involved in the free troposphere from Fig. 5A. For NPF particles of  $\text{H}_2\text{SO}_4$  having a normalized lognormal PSD in the 3- to 200-nm particles size range, at 3.2-km altitude (RH, 60%), the retrieved NPF concentration is in the range of  $10,000 \text{ cm}^{-3}$ , obtained for a solar UV irradiance of  $8 \times 10^{15}$  photons per square centimeter per second. This concentration is in the same range as the one observed during the NPF process in the laboratory experiment. However, in the absence of  $\text{SO}_2$  and PSD measurements, such a comparison must be done with care and only an order of magnitude can be given.

Moreover, from the above Fig. S4 vertical profiles, we evaluated the dust particle number  $N_d$  at 4-km altitude (corresponding to a high dust loading) by computing the dust-backscattering cross-section using the methodology published in ref. 7. An  $N_d$  value equal to  $200 \pm 40 \text{ cm}^{-3}$  was obtained. Assuming  $s$  particles contain sulfate for the backscattering cross-section computation, we found that during nighttime, the  $s$ -particle concentration  $N_s$  reached  $1,000 \pm 250 \text{ cm}^{-3}$  at an altitude of 4 km. Hence, for both  $s$  and  $d$  particles, the retrieved particle-number concentrations are in the same range as in the Beijing field experiment and in the laboratory observations.

- Monge ME, et al. (2012) Alternative pathway for atmospheric particles growth. *Proc Natl Acad Sci USA* 109(18):6840–6844.
- Wagner C, Schuster G, Crowley JN (2009) An aerosol flow tube study of the interaction of  $\text{N}_2\text{O}_5$  with calcite, Arizona dust and quartz. *Atmos Environ* 43(32):5001–5008.
- Wang Q, et al. (2011) Mixing of dust with pollution on the transport path of Asian dust—revealed from the aerosol over Yulin, the north edge of Loess Plateau. *Sci Total Environ* 409(3):573–581.
- Zhang R, Han Z, Cheng T, Tao J (2009) Chemical properties and origin of dust aerosols in Beijing during springtime. *Particuology* 7(1):61–67.
- van Pinxteren D, et al. (2009) Size- and time-resolved chemical particle characterization during CAREBeijing-2006: Different pollution regimes and diurnal profiles. *J. Geophys Res* 114:D00G09.
- Wang Q, et al. (2011) Mixing of dust with pollution on the transport path of Asian dust—revealed from the aerosol over Yulin, the north edge of Loess Plateau. *Sci Total Environ* 409(3):573–581.
- Bzdek BR, Zordan CA, Pennington MR, Luther GW, 3rd, Johnston MV (2012) Quantitative assessment of the sulfuric acid contribution to new particle growth. *Environ Sci Technol* 46(8):4365–4373.
- Winker DM, et al. (2009) Overview of the CALIPSO Mission and CALIOP Data Processing Algorithms. *J Atmos Ocean Technol* 26(11):2310–2323.
- Shimizu A, et al. (2004) Continuous observations of Asian dust and other aerosols by polarization lidars in China and Japan during ACE-Asia. *J Geophys Res* 109: D19S17.
- Ansmann A, et al. (2011) Saharan mineral dust experiments SAMUM-1 and SAMUM-2: What have we learned? *Tellus B Chem Phys Meteorol* 63(4):403–429.
- Tesche M, et al. (2009) Vertically resolved separation of dust and smoke over Cape Verde using multiwavelength Raman and polarization lidars during Saharan Mineral Dust Experiment 2008. *J Geophys Res* 114:D13202.
- Veselovskii I, et al. (2010) Application of randomly oriented spheroids for retrieval of dust particle parameters from multiwavelength lidar measurements. *J Geophys Res* 115:D21203.
- Miffre A, et al. (2012) Interpretation of accurate UV polarization lidar measurements: Application to volcanic ash number concentration retrieval. *J Atmos Ocean Technol* 29(4):558–568.







**Table S2. Iron oxide composition**

|                                | Weight % data from Sigma-Aldrich | Weight % ICP analyses from IRCELYON |
|--------------------------------|----------------------------------|-------------------------------------|
| Fe <sub>2</sub> O <sub>3</sub> | ≥99                              | 99                                  |

**Table S3. Elementary composition of used minerals**

| Samples/element | Fe (%) | Ti (%) | Si (%) | Al (%) | Ca (%) | Mg (%) | K (%) | Na (%) |
|-----------------|--------|--------|--------|--------|--------|--------|-------|--------|
| ATD             | 1.37   | 0.18   | 36.06  | 4.33   | 1.68   | 0.39   | 1.92  | ~1     |
| Iron oxide      | 70.19  | -      | -      | -      | -      | -      | -     | -      |

**Table S4. TSP concentration and PM<sub>1</sub>-to-PM<sub>10</sub> ratios measured at the Wuqing meteorological station (39°23'9"N, 117°1'26"E)**

| Measurement day (month/day/year) | NPF | TSP concentration (µg/m <sup>3</sup> ) | PM <sub>1</sub> /PM <sub>10</sub> |
|----------------------------------|-----|--|-----------------------------------|
| 3/8/2009                         | -   | 256                                    | 0.4                               |
| 3/9/2009                         | +   | 39                                     | 0.6                               |
| 3/12/2009                        | -   | 274                                    | 0.3                               |
| 3/13/2009                        | +   | 23                                     | 0.6                               |
| 3/21/2009                        | -   | 222                                    | 0.3                               |
| 3/22/2009                        | +   | 21                                     | 0.8                               |
| 3/24/2009                        | -   | 88                                     | 0.5                               |
| 3/25/2009                        | +   | 85                                     | 0.6                               |
| 3/26/2009                        | +   | 34                                     | 0.7                               |
| 3/30/2009                        | -   | 156                                    | 0.4                               |
| 3/31/2009                        | +   | 98                                     | 0.3                               |
| 4/01/2009                        | +   | 50                                     | 0.6                               |
| Averaged pre-NPF days            |     | 199 ± 77                               | 0.4 ± 0.1                         |
| Averaged NPF days                |     | 51 ± 28                                | 0.6 ± 0.1                         |

+, yes; -, no.